

A stochastic approach to phase noise analysis for microwaves generated with Kerr optical frequency combs

Fengyu Liu ¹, Curtis R. Menyuk ² & Yanne K. Chembo ¹ 

Kerr optical frequency combs are expected to play a major role in photonic technology, with applications related to spectroscopy, sensing, aerospace, and communication engineering. Most of these applications are related to the metrological performance of Kerr combs, which is ultimately limited by their noise-driven fluctuations. For this reason, it is of high importance to understand the influence of random noise on the comb dynamics. In this communication, we theoretically investigate a model where Gaussian white noise is added to the coupled-mode equations governing the comb dynamics. This stochastic model allows us to characterize the noise-induced broadening of the spectral lines. Moreover, this study permits to determine the phase noise spectra of the microwaves generated via comb photodetection. In this latter case, our analysis indicates that the low-frequency part of the spectra is dominated by pattern drift while the high-frequency part is dominated by pattern deformation. The theoretical results are found to be in excellent agreement with numerical simulations.

¹Department of Electrical and Computer Engineering & Institute for Research in Electronics and Applied Physics (IREAP), University of Maryland, College Park, MD 20742, USA. ²Department of Computer Science and Electrical Engineering, University of Maryland Baltimore County, Baltimore, MD 21250, USA. email: ykchembo@umd.edu

Kerr optical frequency combs are sets of discrete and equidistant spectral lines that can be generated using a high- Q monolithic resonator pumped with a resonant laser^{1,2}. When the bulk medium of the cavity features a Kerr nonlinearity, the pump photons can be frequency-converted via four-wave mixing and populate adjacent cavity eigenmodes^{3,4}. A key characteristic of these combs is that there is a threshold pump power below which this four-wave mixing process is spontaneous, and above which it is stimulated. In this latter case, the comb lines exhibit strong phase correlation in the spectral domain. Such phase-locking leads to the formation of well-defined patterns in the spatiotemporal domain, which can be extended (such as roll patterns), or localized (bright or dark solitons). From a theoretical viewpoint, Kerr combs have been studied extensively and their deterministic characteristics are nowadays well understood⁵⁻⁷.

Kerr optical frequency combs have been found in numerous applications such as coherent optical communications⁸, spectroscopy⁹, sensing^{10,11}, and ultra-pure microwave generation¹². Most of these applications are based on the exceptional coherence of the combs, which is ultimately limited by noise-driven fluctuations. Compared with other frequency comb generation systems, Kerr comb generators are simpler and more compact because of the small mode volume, high photon density, and long photon lifetime, but these advantages may introduce more noise. Researchers have studied various noises in the resonator theoretically and experimentally¹³⁻¹⁵. However, the mechanism by which these noises affect the fluctuations, and further the phase noise of the combs, remains unclear. One approach to understanding the effect of these fluctuations is to introduce Langevin noise terms leading to stochastic differential equations.

In this communication, we aim at using this stochastic approach in order to characterize the coherence of the combs in the optical domain. We focus on the case of additive Gaussian noise because despite its conceptual simplicity, it already unveils a complex interaction between nonlinearity and noise that leads to profound consequences in terms of metrological performance. We also focus on whispering-gallery mode resonators here because of their conceptual simplicity and practical importance. This analysis will allow us to understand how the fluctuations of the optical comb lines are converted to microwave phase noise after the photodetection of the comb. We anticipate that our results can be extended to more complex resonators with high quality factors and more complex noise spectra.

Results and discussion

System. The main element of the system is a whispering-gallery mode resonator of main radius a , pumped with a resonant and continuous-wave laser of power P_L and angular frequency ω_L . The size of the resonator defines its free-spectral range (FSR) as $F_R = 1/T_R = \Omega_R/2\pi = v_g/2\pi a = c/2\pi a n_g$, where Ω_R is the angular FSR, c is the velocity of light in vacuum, n_g is the group-velocity refraction index at the pump wavelength, and $v_g = c/n_g$ is the corresponding group velocity. The photons are trapped in eigenmodes with effective volume $V_{\text{eff}} = 2\pi a A_{\text{eff}}$, with A_{eff} being the effective mode area. These modes are longitudinal eigenmodes from the same transverse mode family, which are labeled with their reduced azimuthal eigenumber l such that $l=0$ is the laser-pumped mode and the sidemodes are expanded as $l = \pm 1, \pm 2, \pm 3, \dots$. The corresponding eigenfrequencies can be Taylor-expanded as $\omega_l = \omega_0 + \sum_{n=1}^{+\infty} \zeta_n l^n / n!$, where ω_0 is the eigenfrequency of the laser-pumped mode, $\zeta_1 = \Omega_R$, while ζ_n is the n th-order dispersion coefficient for $n \geq 2$. The losses in the resonator are characterized by the half-linewidth $\kappa = \omega_L/2Q$, where Q is the total (or loaded) quality factor. In fact, the loaded

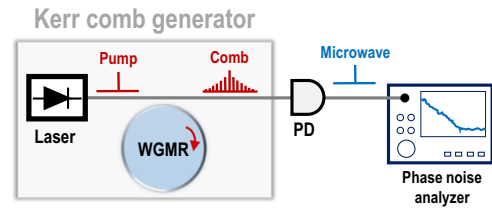


Fig. 1 Schematic illustration of microwave generation using a Kerr optical frequency comb. WGMR whispering-gallery mode resonator, PD photodiode.

quality factor depends on the intrinsic (or cavity) and extrinsic (or coupling) quality factors as $Q^{-1} = Q_i^{-1} + Q_t^{-1}$, leading to $\kappa = \kappa_i + \kappa_t$. The bulk material of this optical cavity has a Kerr coefficient n_2 , which can be rescaled to $\gamma = \omega_L n_2 / c A_{\text{eff}}$ (in units of $W^{-1}m^{-1}$). A schematic representation of the experimental system is presented in Fig. 1.

Stochastic model. The semi-classical dynamics of Kerr optical frequency combs can be investigated using two equivalent models, namely the coupled-mode equations^{16,17} and the Lugiato-Lefever spatiotemporal equation¹⁸⁻²¹. The most suitable model for our analysis is the first one because we need to resolve the noise-driven fluctuations for each optical mode. In that case, the temporal dynamics of the modal amplitudes of the various modes obey the following equations:

$$\begin{aligned} \dot{\mathcal{E}}_l = & -\kappa \mathcal{E}_l + i \left[\sigma - \sum_{k=2}^{k_{\text{max}}} \frac{\zeta_k}{k!} l^k \right] \mathcal{E}_l \\ & + i v_g \gamma \sum_{m,n,p} \delta(m-n+p-l) \mathcal{E}_m \mathcal{E}_n^* \mathcal{E}_p \\ & + \delta(l) \sqrt{2\kappa_t/T_R} \sqrt{P_L} + \sqrt{2\kappa} \Lambda v_l(t), \end{aligned} \quad (1)$$

where $\mathcal{E}_l(t)$ is a complex slowly varying amplitude for each mode l and is normalized such that $|\mathcal{E}_l|^2$ is in units of watts. The parameter $\sigma = \omega_L - \omega_0$ corresponds to the detuning between the laser and the pumped resonance frequency. The complex-valued additive Gaussian white noise terms $v_l(t)$ have the correlation properties

$$\langle v_l(t) \rangle = 0, \quad (2)$$

$$\langle v_l(t) v_l^*(t') \rangle = \delta_{l,l'} \delta(t-t'), \quad (3)$$

where the delta symbols with subscripts represent Kronecker functions while the delta symbols followed by parentheses represent Dirac delta functions. These noise terms are weighted in each mode by the real-valued amplitude Λ which is such that Λ^2 is in unit of watts. This approach of coupled-mode equations with additive Gaussian noise was introduced in ref. ²², and some statistical properties of the comb had been analytically derived. It should be noted that the coherence of the combs can also be analyzed from a purely spatiotemporal perspective⁸.

The output optical field $\mathcal{E}_{\text{out},l}$ is related to the intra-cavity field by

$$\mathcal{E}_{\text{out},l} = \sqrt{2\kappa_t T_R} \mathcal{E}_l - \sqrt{P_L} \delta(l), \quad (4)$$

still with $|\mathcal{E}_{\text{out},l}|^2$ in units of watts.

We use the following parameters for our numerical simulations: The single-frequency laser is assumed to be ideal with an infinitely narrow linewidth at wavelength $\lambda_0 = 1550$ nm. The refraction index of the resonator at that frequency is $n_g = 1.43$, corresponding to $\Omega_R = 2\pi \times 13.4$ GHz. The nonlinear parameter is set to $\gamma = 1.0$ $W^{-1}km^{-1}$. The intrinsic quality factor is $Q_i = 10^9$, and the coupling quality factor is $Q_t = 0.25 \times 10^9$.

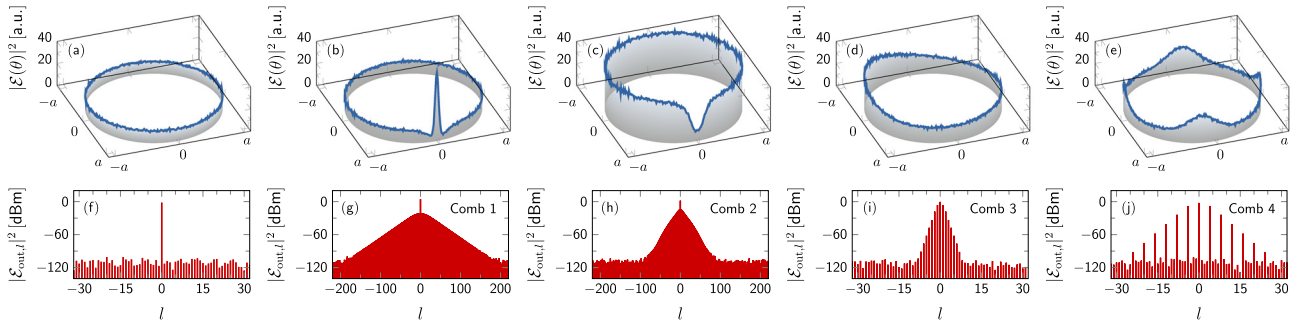


Fig. 2 Schematic representation of stochastic Kerr combs. The combs are in space (a–e) and frequency (f–j), and are at a given time t (snapshot), after simulation of Eq. (1). The upper row displays the total intracavity field power $|\mathcal{E}(\theta)|^2$, while the lower row displays the corresponding stem plot for the modal intensities $|\mathcal{E}_{\text{out},l}|^2$ in a logarithmic scale (note that they are spatiotemporal snapshots and not Fourier spectra). The noise in the spatiotemporal patterns has been accentuated for the sake of visual clarity. **a, f** Flat state (no comb). **b, g** Bright soliton ($P_L = 4.00$ mW, $\sigma = -2\kappa$, and $\zeta_2 = 2\pi \times 2.92$ kHz). **c, h** Dark soliton ($P_L = 5.30$ mW, $\sigma = -2.5\kappa$, and $\zeta_2 = -2\pi \times 2.92$ kHz). **d, i** Roll pattern of order $L = 1$ ($P_L = 3.09$ mW, $\sigma = -\kappa$, and $\zeta_2 = 2\pi \times 874.7$ kHz). **e, j** Roll pattern of order $L = 4$ ($P_L = 2.27$ mW, $\sigma = -\kappa$, and $\zeta_2 = 2\pi \times 366.4$ kHz). The numerical simulations will involve the four cases from Comb 1 to Comb 4.

The additive Gaussian noise amplitude is $\Lambda = 5 \times 10^{-6} \text{ W}^{1/2}$. We neglect dispersion beyond the second order.

Simulation of Eq. (1) yields a variety of solutions depending on the system parameters and initial conditions. These solutions for \mathcal{E}_l lead to distinctive intracavity spatiotemporal patterns, as shown in Fig. 2. In this communication, we will focus on four different patterns, namely bright solitons, dark solitons, roll patterns with single-FSR spacing, and roll patterns with multiple-FSR spacing. Throughout the article, we assume that the system is in a stationary and noise-free state for $t < 0$, while the noise is switched on at $t = 0$ and the system thereby becomes stochastic.

Optical fluctuations under threshold. In the sub-threshold regime, all the sidemodes $l \neq 0$ are fluctuating around zero, while the amplitude of the central mode $l = 0$ fluctuates around a non-zero amplitude. The fields can therefore be rewritten as

$$\mathcal{E}_l(t) = \begin{cases} \mathcal{E}_0(0) + \delta\mathcal{E}_0(t) & \text{for } l = 0 \\ \delta\mathcal{E}_l(t) & \text{for } l \neq 0 \end{cases}, \quad (5)$$

where $\delta\mathcal{E}_l$ denotes the fluctuation fields, while the amplitude $\mathcal{E}_0(0)$ is the solution of the nonlinear algebraic equation

$$0 = -\kappa\mathcal{E}_0(0) + i\left[\sigma - \frac{\zeta_2}{2}l^2\right]\mathcal{E}_0(0) + iv_g\gamma|\mathcal{E}_0(0)|^2\mathcal{E}_0(0) + \sqrt{2\kappa_\tau/T_R}\sqrt{P_L}. \quad (6)$$

If we consider N sidemode pairs around the central mode, Eq. (1) can be rewritten as a set of $2N + 1$ differential equations after ignoring the multiplicative fluctuation terms, in the form

$$\dot{\delta\mathcal{E}}_l = \mathcal{R}_l\delta\mathcal{E}_l + \mathcal{S}_l\delta\mathcal{E}_{-l}^* + \sqrt{2\kappa}\Lambda v_l(t) \quad (7)$$

for the fluctuations in each mode, with

$$\mathcal{R}_l = -\kappa + i\left[\sigma - \frac{\zeta_2}{2}l^2\right] + 2iv_g\gamma|\mathcal{E}_0(0)|^2, \quad (8)$$

$$\mathcal{S}_l = iv_g\gamma\mathcal{E}_0^2(0), \quad (9)$$

being complex-valued parameters. Since the fluctuations are pairwise coupled, Eq. (7) can be further rewritten as $N + 1$ independent sets of 2×2 noise-driven linear flows, in the form

$$\begin{bmatrix} \dot{\delta\mathcal{E}}_l \\ \dot{\delta\mathcal{E}}_{-l}^* \end{bmatrix} = \mathbf{J}_l \begin{bmatrix} \delta\mathcal{E}_l \\ \delta\mathcal{E}_{-l}^* \end{bmatrix} + \sqrt{2\kappa}\Lambda \begin{bmatrix} v_l(t) \\ v_{-l}^*(t) \end{bmatrix}, \quad (10)$$

where

$$\mathbf{J}_l = \begin{bmatrix} \mathcal{R}_l & \mathcal{S}_l \\ \mathcal{S}_l^* & \mathcal{R}_l^* \end{bmatrix} \quad (11)$$

is a 2×2 Jacobian matrix. These equations can be solved in the Fourier domain as

$$\begin{bmatrix} \delta\tilde{\mathcal{E}}_l(\omega) \\ \delta\tilde{\mathcal{E}}_{-l}^*(-\omega) \end{bmatrix} = -\sqrt{2\kappa}\Lambda[\mathbf{J}_l - i\omega\mathbf{I}_2]^{-1} \begin{bmatrix} \tilde{v}_l(\omega) \\ \tilde{v}_{-l}^*(-\omega) \end{bmatrix}, \quad (12)$$

where \mathbf{I}_2 is a 2nd order identity matrix, and the solution is given by

$$\delta\tilde{\mathcal{E}}_l(\omega) = \sqrt{2\kappa}\Lambda \frac{(\mathcal{R}_l^* - i\omega)\tilde{v}_l(\omega) - \mathcal{S}_l\tilde{v}_{-l}^*(-\omega)}{D_l(\omega)}, \quad (13)$$

where

$$D_l(\omega) = (\mathcal{R}_l - i\omega)(\mathcal{R}_l^* - i\omega) - \mathcal{S}_l\mathcal{S}_l^* = (\kappa^2 + \eta_l^2 - v_g^2\gamma^2|\mathcal{E}_0(0)|^4 - \omega^2) + 2i\kappa\omega, \quad (14)$$

$$\eta_l = \Im[\mathcal{R}_l] = \sigma - \frac{\zeta_2}{2}l^2 + 2v_g\gamma|\mathcal{E}_0(0)|^2. \quad (15)$$

The spectral density of the fluctuations for the output field in the mode l then becomes

$$\begin{aligned} S_{\delta\mathcal{E},l}(\omega) &= 2\kappa_\tau T_R (\delta\tilde{\mathcal{E}}_l(\omega)\delta\tilde{\mathcal{E}}_l^*(\omega)) \\ &= 4\kappa_\tau\kappa T_R \Lambda^2 \\ &\quad \times \frac{\omega^2 + 2\eta_l\omega + \kappa^2 + \eta_l^2 + v_g^2\gamma^2|\mathcal{E}_0(0)|^4}{(\kappa^2 + \eta_l^2 - v_g^2\gamma^2|\mathcal{E}_0(0)|^4 - \omega^2)^2 + 4\kappa^2\omega^2}. \end{aligned} \quad (16)$$

Using the above equation and Parseval's theorem, the variance of the fluctuations can be written as

$$\begin{aligned} \langle |\delta\mathcal{E}_{\text{out},l}|^2 \rangle &= \frac{1}{2\pi} \int_{-\infty}^{+\infty} S_{\delta\mathcal{E},l}(\omega) d\omega \\ &= \frac{2\kappa_\tau T_R \Lambda^2 (\kappa^2 + \eta_l^2)}{\kappa^2 - v_g^2\gamma^2|\mathcal{E}_0(0)|^4 + \eta_l^2}. \end{aligned} \quad (17)$$

The above formula is valid as long as the sidemodes remain noise-driven, i.e., when the real parts of eigenvalues of the Jacobian \mathbf{J}_l are strictly negative following the condition $v_g^2\gamma^2|\mathcal{E}_0(0)|^4 < \kappa^2 + \eta_l^2$. We note that the noise amplitude parameter Λ is defined such that $\langle |\mathcal{E}_l(t)|^2 \rangle \rightarrow \Lambda^2$ when $\sqrt{P_L} \rightarrow 0$, so

Λ^2 equals the intracavity power of the sidemodes in the hypothetical case where they are exclusively driven by external noise.

Microcomb above threshold: fluctuations from pattern drift and pattern deformation. When the power of the external laser pump field is set above threshold, some sidemode pairs can be deterministically excited, thereby leading to Kerr comb formation. These combs correspond to various spatiotemporal patterns inside the cavity, as shown by Fig. 2. Here, we aim at analyzing the dynamics of fluctuations generated by the additive Gaussian white noise on these patterns.

The first step is to note that the unitary symmetry of Eq. (1) indicates that the phase of the stationary side modes is arbitrary because of the invariance of Eq. (1) under phase rotation

$$\mathcal{E}_l(0) \rightarrow \mathcal{E}_l(0) \exp(il\vartheta) \quad (18)$$

for all l and with arbitrary ϑ . In other words, the system is neutrally stable in the azimuthal direction. This corresponds to a shift of the entire azimuthal profile by a constant angle ϑ . As a result of this invariance, the Jacobian of the coupled mode equations has a null eigenvalue. The effect of this mode is to induce a pattern drift that undergoes a random walk in the azimuthal direction. In other words, whenever a pattern is stochastically perturbed in the azimuthal direction, the perturbation is undamped and can diverge asymptotically – Indeed, further analysis will show that this is a Wiener process. This phenomenon is referred to as timing jitter in systems where the output signal is analyzed as an unwrapped timetrace instead of a stationary pattern^{23–25}. As a result of this drift, the traditional perturbation methods that assume small deviations are invalid.

To circumvent this problem, we rewrite the field in each mode as

$$\mathcal{E}_l(t) = \mathcal{E}_l(0) \exp[i l \vartheta(t)] + \delta \mathcal{E}_l(t), \quad (19)$$

where $\vartheta(t)$ is the global phase deviation of the comb with $\vartheta(0) = 0$ – Note that the complex-valued amplitude fluctuations are also initialized as $\delta \mathcal{E}_l(0)$. The complex-valued perturbations $\delta \mathcal{E}_l$ are referred to as orbital deviations, and they represent the deviation from the orbit of the stationary solution²⁶. These perturbations are associated to eigenvalues with strictly negative real parts, and for that reason, are damped. As a consequence, the fluctuations $\delta \mathcal{E}_l$ are small at all time and they lead to pattern deformation, i.e., small stochastic fluctuations of the shape of the spatiotemporal pattern. The effect of pattern drift and deformation will be evaluated via their corresponding phase noise spectra. A schematic representation of pattern drift and pattern deformation is displayed in Fig. 3.

Optical stochastic fluctuations of soliton patterns. In the case of bright and dark solitons, all of the sidemodes adjacent to the pumped mode are excited. As a consequence, all the related field fluctuations have to be accounted for, and they will be globally coupled. The variable $\mathcal{E}_l(0)$ can be numerically calculated by solving the equations

$$\begin{aligned} 0 = & -\kappa \mathcal{E}_l(0) + i \left[\sigma - \frac{\zeta_2}{2} l^2 \right] \mathcal{E}_l(0) \\ & + i v_g \gamma \sum_{m,n,p} \delta(m-n+p-l) \mathcal{E}_m(0) \mathcal{E}_n^*(0) \mathcal{E}_p(0) \\ & + \delta(l) \sqrt{2\kappa_i/T_R} \sqrt{P_L} \end{aligned} \quad (20)$$

and choosing an appropriate phase.

Substituting Eq. (19) into Eq. (1), and ignoring the terms for multiplication of fluctuations, we get the set of $2N + 1$ differential

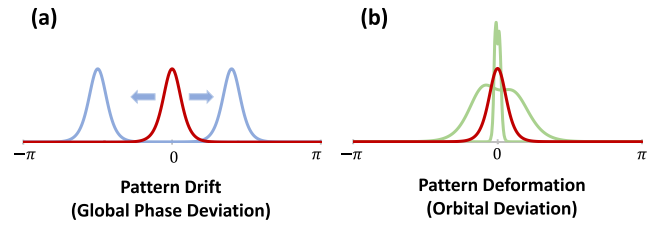


Fig. 3 Schematic illustration of pattern drift and pattern deformation.

a Schematic illustration of pattern drift for a soliton. The red curve represents the initial unperturbed soliton, while the blue curves represent the perturbed solitons with pattern drift. **b** Schematic illustration of pattern deformation for a soliton. The red curve represents the initial unperturbed soliton, while the green curves represent the perturbed solitons with pattern deformation. Pattern drift corresponds to a translational change of the soliton’s azimuthal position within the cavity. On the other hand, pattern deformation corresponds to a change of the soliton’s shape. Our analysis shows that pattern drift is the leading contribution to phase noise at low-frequency offset from the carrier, while pattern deformation is the leading contribution to phase noise at high-frequency offset.

equations again:

$$i l \mathcal{E}_l(0) \exp(i l \vartheta) \dot{\vartheta} + \delta \dot{\mathcal{E}}_l = \sum_{p=-N}^N R_{l,p} \delta \mathcal{E}_p + \sum_{p=-N}^N S_{l,p} \delta \mathcal{E}_p^* + \sqrt{2\kappa} \Lambda v_l(t) \quad (21)$$

for the fluctuations in each mode, where

$$\begin{aligned} \mathcal{R}_{l,p}(t) = & \left[-\kappa + i \left(\sigma - \frac{\zeta_2}{2} l^2 \right) \right] \delta(p-l) \\ & + 2i v_g \gamma \sum_{m,n} \delta(m-n+p-l) \mathcal{E}_m(0) \mathcal{E}_n^*(0) \\ & \times \exp[i(l-p)\vartheta(t)] \end{aligned} \quad (22)$$

$$\begin{aligned} \mathcal{S}_{l,p}(t) = & i v_g \gamma \sum_{m,n} \delta(m+n-p-l) \mathcal{E}_m(0) \mathcal{E}_n(0) \\ & \times \exp[i(l+p)\vartheta(t)] \end{aligned} \quad (23)$$

are complex-valued parameters determined by the initial stationary solutions and the global phase deviation.

We can rewrite Eq. (21) under the form of a noise-driven flow, in the form

$$\begin{bmatrix} \mathbf{X} \\ \mathbf{X}^* \end{bmatrix} \dot{\vartheta} + \begin{bmatrix} \delta \dot{\Psi} \\ \delta \dot{\Psi}^* \end{bmatrix} = \mathbf{J}(t) \begin{bmatrix} \delta \Psi \\ \delta \Psi^* \end{bmatrix} + \begin{bmatrix} \mathbf{V}(t) \\ \mathbf{V}^*(t) \end{bmatrix}, \quad (24)$$

where the Jacobian $\mathbf{J}(t)$ is given by the following square matrix of order $(4N + 2)$

$$\mathbf{J}(t) = \begin{bmatrix} \mathbf{R}(t) & \mathbf{S}(t) \\ \mathbf{S}^*(t) & \mathbf{R}^*(t) \end{bmatrix}, \quad (25)$$

while the $(2N + 1)$ -dimensional vectors involved in this flow are explicitly defined as

$$\delta \Psi(t) = \begin{bmatrix} \delta \mathcal{E}_{-N}(t) \\ \vdots \\ \delta \mathcal{E}_{+N}(t) \end{bmatrix}, \quad (26)$$

$$\mathbf{V}(t) = \sqrt{2\kappa} \Lambda \begin{bmatrix} v_{-N}(t) \\ \vdots \\ v_{+N}(t) \end{bmatrix}, \quad (27)$$

and

$$\mathbf{X}(t) = \begin{bmatrix} -iN\mathcal{E}_{-N}(0) \exp[-iN\vartheta] \\ -i(N-1)\mathcal{E}_{-(N-1)}(0) \exp[-i(N-1)\vartheta] \\ \vdots \\ -i\mathcal{E}_{-1}(0) \exp[-i\vartheta] \\ 0 \\ i\mathcal{E}_1(0) \exp[i\vartheta] \\ \vdots \\ i(N-1)\mathcal{E}_{N-1}(0) \exp[i(N-1)\vartheta] \\ iN\mathcal{E}_N(0) \exp[iN\vartheta] \end{bmatrix}. \quad (28)$$

It should be noted that the Jacobian matrix $\mathbf{J}(t)$ has to be determined numerically because its components depend on the stationary state values of the semi-classical modal fields $\mathcal{E}_l(0)$. This Jacobian matrix is diagonalizable as

$$\mathbf{J}(t) = \mathbf{W}(t) \mathbf{D} \mathbf{P}(t), \quad (29)$$

where $\mathbf{W}(t)$ is the matrix composed by the eigenvectors of $\mathbf{J}(t)$, \mathbf{D} is a constant diagonal matrix composed of the eigenvalues of $\mathbf{J}(t)$, and $\mathbf{P}(t)$ is the inverse of $\mathbf{W}(t)$. It is important to note that owing to the symmetry properties of $\mathbf{J}(t)$, \mathbf{D} is a time-independent matrix, while $\mathbf{P}(t)$ and $\mathbf{W}(t)$ are time-dependent.

Using Eq. (18), one can see one of the eigenvectors of the Jacobian $\mathbf{J}(t)$ is

$$\mathbf{w}_1(t) = C \begin{bmatrix} \mathbf{X}(t) \\ \mathbf{X}^*(t) \end{bmatrix} \exp(i\alpha_0), \quad (30)$$

where

$$C = \frac{1}{\sqrt{2 \sum_{l=-N}^N l^2 |\mathcal{E}_l(0)|^2}} \quad (31)$$

is the normalization factor that leads to $|\mathbf{w}_1|^2 = 1$, while α_0 is a real-valued constant. This solution associated to the eigenvalue 0 is generally referred to as the Goldstone mode. Without loss of generality, we define $\mathbf{w}_1(t)$ as the first column vector in matrix $\mathbf{W}(t)$, 0 as the first diagonal element in the matrix \mathbf{D} and $\mathbf{p}_1(t)$ as the first row vector in the matrix $\mathbf{P}(t)$.

It now appears that each row of the matrix $\mathbf{W}(t)$ and each column of the matrix $\mathbf{P}(t)$ have the same temporal dependence. For example, the time dependence of any element in the first row of $\mathbf{W}(t)$ is the same as the time dependence of $W_{1,1}$, which is $\exp[-iN\vartheta]$ as shown in Eq. (28). Correspondingly, the time dependence of any element in the first column of $\mathbf{P}(t)$ is the same as the time dependence of $P_{1,1}$, which is $\exp[iN\vartheta]$. Since $\mathbf{P}(t)$ is the inverse of $\mathbf{W}(t)$, the relations between these vectors are given by:

$$\mathbf{p}_m(t) \cdot \mathbf{w}_n(t) = \begin{cases} 1 & \text{for } m = n \\ 0 & \text{for } m \neq n \end{cases}. \quad (32)$$

Substituting Eqs. (29) and (30) into Eq. (24), the dynamical flow can be linearly transformed into the new form

$$\frac{\exp(-i\alpha_0)}{C} \mathbf{P}(t) \mathbf{w}_1(t) \dot{\vartheta} + \delta\dot{\Phi} = \mathbf{D} \delta\Phi + \mathbf{Z}(t), \quad (33)$$

where we have introduced

$$\delta\Phi = \mathbf{P}(t) \begin{bmatrix} \delta\Psi \\ \delta\Psi^* \end{bmatrix} = \begin{bmatrix} \delta\phi_1(t) \\ \vdots \\ \delta\phi_{(4N+2)}(t) \end{bmatrix} \quad (34)$$

and

$$\mathbf{Z}(t) = \mathbf{P}(t) \begin{bmatrix} \mathbf{V}(t) \\ \mathbf{V}^*(t) \end{bmatrix} = \begin{bmatrix} z_1(t) \\ \vdots \\ z_{(4N+2)}(t) \end{bmatrix}. \quad (35)$$

The correlation properties of these new stochastic variables can be calculated as

$$\Xi_{m,n} = \langle z_m^*(t) z_n(t) \rangle = 2\kappa\Lambda^2 \sum_{i=1}^{4N+2} \langle \mathcal{P}_{m,i}^* \mathcal{P}_{n,i} \rangle. \quad (36)$$

Since all columns in the matrix $\mathbf{P}(t)$ have the same dependence on time t , we can see that the quantity $\mathcal{P}_{m,i}^* \mathcal{P}_{n,i}$ is invariant, i.e.

$$\mathcal{P}_{m,i}^*(t) \mathcal{P}_{n,i}(t) = \text{Constant}. \quad (37)$$

Eq. (33) describes a $4N+2$ -dimensional set of dynamical equations in the diagonal space. The first one of these equations can be written as

$$\frac{\exp(-i\alpha_0)}{C} \dot{\vartheta} + \delta\dot{\phi}_1 = z_1(t), \quad (38)$$

which is a Wiener process, because the first element of the diagonal matrix \mathbf{D} is null. Since $\delta\phi_1$ represents the weight of the orbital deviation on the stationary solution orbit, we have to select

$$\dot{\vartheta} = C \exp(i\alpha_0) z_1(t) \quad \text{and} \quad \delta\dot{\phi}_1 = 0, \quad (39)$$

and set the value of $\delta\phi_1$ to 0. This means that although we initially introduced $4N+3$ variables ($2N+1$ orbital deviations \mathcal{E}_l , their $2N+1$ conjugates, and global phase deviation ϑ), the total number of degrees of freedom for this system is still $4N+2$.

The other dynamical equations embedded in Eq. (33) describe a set of $(4N+1)$ Ornstein-Uhlenbeck processes driven by additive Gaussian white noises. The correlation properties of the linearly transformed modes are given by

$$\Pi_{m,n} = \langle \delta\phi_m^*(t) \delta\phi_n(t) \rangle = 0 \quad (40)$$

for the cases that $m=1$ or $n=1$, and

$$\Pi_{m,n} = \langle \delta\phi_m^*(t) \delta\phi_n(t) \rangle = -\frac{\Xi_{m,n}}{\mathcal{D}_{m,m}^* + \mathcal{D}_{n,n}} \quad (41)$$

for any other cases, where $\mathcal{D}_{i,i}$ is the i th diagonal element of the matrix \mathbf{D} .

The orbital deviation field $\delta\mathcal{E}_l(t)$ can now be recovered from $\delta\Phi$ via an inverse linear transformation, and the variance of this fluctuation is given by

$$\langle |\delta\mathcal{E}_l(t)|^2 \rangle = \sum_{m,n} \mathcal{W}_{l+N+1,m}^* \mathcal{W}_{l+N+1,n} \Pi_{m,n}. \quad (42)$$

The results of this orbital deviation analysis in solitons are presented in Fig. 4a, b and display an excellent agreement with numerical simulations.

Optical stochastic fluctuations of roll patterns. For roll patterns of order L , the main steps of the previous analysis as developed for solitons remain valid. Accounting for the fact that not all of the sidemodes are excited, the modal fields of the roll pattern can be written as

$$\mathcal{E}_l(t) = \begin{cases} \mathcal{E}_l(0) \exp(il\vartheta(t)) + \delta\mathcal{E}_l(t) & \text{for } l = nL \\ \delta\mathcal{E}_l(t) & \text{for } l \neq nL \end{cases}, \quad (43)$$

where n is an integer. After neglecting higher-order stochastic terms, we obtain an equation analogous to Eq. (24), but now the $(4N+2)$ -dimensional Jacobian

$$\mathbf{J}(t) = \begin{bmatrix} \mathbf{R}(t) & \mathbf{S}(t) \\ \mathbf{S}^*(t) & \mathbf{R}^*(t) \end{bmatrix} \quad (44)$$

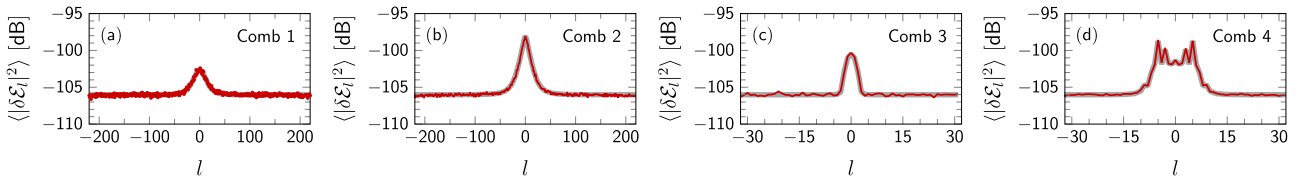


Fig. 4 Variance of orbital deviation of the intra-cavity field. The figure shows the results of **a** bright soliton (Comb 1), **b** dark soliton (Comb 2), **c** roll pattern of order $L = 1$ (Comb 3), and **d** roll pattern of order $L = 4$ (Comb 4) displayed in Fig. 2 as a function of the sidemode order l , respectively. The thick gray curves correspond to analytical results obtained from Eqs. (42), (66), and (67), while the thin red curves result from the simulations of Eq. (1). One can note the excellent agreement between analytical and numerical results.

is defined with the complex-valued elements

$$\mathcal{R}_{l,p}(t) = \left[-\kappa + i \left(\sigma - \frac{\zeta_2}{2} l^2 \right) \right] \delta(p - l) + 2iv_g \gamma \sum_{m,n} \delta(mL - nL + p - l) \mathcal{E}_{mL}(0) \mathcal{E}_{nL}^*(0) \times \exp[i(l - p)\vartheta(t)], \quad (45)$$

$$\mathcal{S}_{l,p}(t) = iv_g \gamma \sum_{m,n} \delta(mL + nL - p - l) \mathcal{E}_{mL}(0) \mathcal{E}_{nL}(0) \times \exp[i(l + p)\vartheta(t)], \quad (46)$$

which are determined by the deterministic (ideally noiseless) stationary roll pattern.

Since only sidemodes l that are multiples of L are excited, Eqs. (45) and (46) indicate that the Jacobian becomes block diagonal, and we can reorder this Jacobian to make the q th block \mathbf{J}_q correspond to the Bloch modes with wavenumber q , namely $\delta\mathcal{E}_{pL \pm q}$ with p being an integer²⁷. Without loss of generality, we consider M excited modes on each side and the non-excited adjacent modes, which includes the mode l when it fulfills the condition $-(ML + L/2) < l \leq ML + L/2$. If L is an odd number, there are $(L + 1)/2$ blocks in the Jacobian matrix, with the label q being from 0 to $(L - 1)/2$. The Jacobian \mathbf{J}_0 is a matrix of order $2(2M + 1)$, and the other blocks are matrices of order $4(2M + 1)$. If L is an even number, there are $L/2 + 1$ blocks in the Jacobian matrix (from 0 to $L/2$), where \mathbf{J}_0 and $\mathbf{J}_{L/2}$ are matrices of order $2(2M + 1)$, and the other blocks are matrices of order $4(2M + 1)$.

We can now treat the equations associated with the various blocks separately. Consequently, Eq. (21) can be rewritten under the form of several noise-driven flows, in the form

$$\delta(q) \begin{bmatrix} \mathbf{X}_0 \\ \mathbf{X}_0^* \end{bmatrix} \dot{\vartheta} + \begin{bmatrix} \delta\dot{\Psi}_q \\ \delta\dot{\Psi}_q^* \end{bmatrix} = \mathbf{J}_q \begin{bmatrix} \delta\Psi_q \\ \delta\Psi_q^* \end{bmatrix} + \begin{bmatrix} \mathbf{V}_q(t) \\ \mathbf{V}_q^*(t) \end{bmatrix}. \quad (47)$$

From these equations, we can obtain vectors of order $2(2M + 1)$ for the field and external noise fluctuations either for the case $q = 0$ or for the case $q = L/2$ when L is even, in the form

$$\delta\Psi_q(t) = \begin{bmatrix} \delta\mathcal{E}_{-(ML+q)}(t) \\ \vdots \\ \delta\mathcal{E}_{ML+q}(t) \end{bmatrix}, \quad (48)$$

$$\mathbf{V}_q(t) = \sqrt{2\kappa\Lambda} \begin{bmatrix} v_{-(ML+q)}(t) \\ \vdots \\ v_{ML+q}(t) \end{bmatrix}. \quad (49)$$

For all the other cases, the $4(2M + 1)$ -dimensional fluctuation and noise vectors are explicitly expressed as

$$\delta\Psi_q(t) = \begin{bmatrix} \delta\mathcal{E}_{-(ML+q)}(t) \\ \vdots \\ \delta\mathcal{E}_{ML+q}(t) \\ \delta\mathcal{E}_{-(ML-q)}(t) \\ \vdots \\ \delta\mathcal{E}_{ML-q}(t) \end{bmatrix}, \quad (50)$$

$$\mathbf{V}_q(t) = \sqrt{2\kappa\Lambda} \begin{bmatrix} v_{-(ML+q)}(t) \\ \vdots \\ v_{ML+q}(t) \\ v_{-(ML-q)}(t) \\ \vdots \\ v_{ML-q}(t) \end{bmatrix}. \quad (51)$$

The Jacobian and all the blocks $\mathbf{J}_q(t)$ are diagonalizable. Hence, they can be written as

$$\mathbf{J}_q(t) = \mathbf{W}_q(t) \mathbf{D}_q \mathbf{P}_q(t), \quad (52)$$

where \mathbf{D}_q is a constant diagonal matrix, while $\mathbf{W}_q(t)$ and $\mathbf{P}_q(t)$ are time-dependent.

The real part of the eigenvalues for every block is always negative, except for the one for the 0th block. We can see that 0 is also one of the eigenvalues of \mathbf{J}_0 , and the corresponding eigenvector $\mathbf{w}_1^{(0)}$ can be written as the following vector of order $4M + 2$:

$$\mathbf{w}_1^{(0)} = C \begin{bmatrix} \mathbf{X}_0(t) \\ \mathbf{X}_0^*(t) \end{bmatrix} \exp(i\alpha_0), \quad (53)$$

where

$$\mathbf{X}_0(t) = \begin{bmatrix} -iML\mathcal{E}_{-ML}(0) \exp[-iML\vartheta] \\ -i(M - 1)L\mathcal{E}_{-(M-1)L}(0) \exp[-i(M - 1)L\vartheta] \\ \vdots \\ -iL\mathcal{E}_{-L}(0) \exp[-iL\vartheta] \\ 0 \\ iL\mathcal{E}_L(0) \exp[iL\vartheta] \\ \vdots \\ i(M - 1)L\mathcal{E}_{(M-1)L}(0) \exp[i(M - 1)L\vartheta] \\ iML\mathcal{E}_N(0) \exp[iML\vartheta] \end{bmatrix} \quad (54)$$

is defined in a similarly way as Eq. (28), while

$$C = \frac{1}{\sqrt{2\sum_{m=-M}^M m^2 L^2 |\mathcal{E}_{mL}(0)|^2}} \quad (55)$$

is the normalization factor with α_0 being a real-valued constant phase. We still assume that $\mathbf{w}_1^{(0)}$ is the first column vector in the matrix \mathbf{W}_0 , where \mathbf{W}_0 is the inverse of \mathbf{P}_0 . The first diagonal element in matrix \mathbf{D}_0 is null, and the first row vector in matrix \mathbf{P}_0 is $\mathbf{p}_1^{(0)}$.

We can now process each block in the same way as in the previous subsection. In the diagonal space, the 0th flow is linearly transformed into

$$\frac{\exp(-i\alpha_0)}{C} \mathbf{P}_0(t) \mathbf{w}_1^{(0)}(t) \dot{\vartheta} + \delta \dot{\Phi}_0 = \mathbf{D}_0 \delta \Phi_0 + \mathbf{Z}_0(t), \quad (56)$$

and the other flows ($q = 1, 2, \dots$) are transformed into

$$\delta \dot{\Phi}_q = \mathbf{D}_q \delta \Phi_q + \mathbf{Z}_q(t), \quad (57)$$

with

$$\delta \Phi_q = \mathbf{P}_q(t) \begin{bmatrix} \delta \Psi_q \\ \delta \Psi_q^* \end{bmatrix} = \begin{bmatrix} \delta \phi_{q,1}(t) \\ \delta \phi_{q,2}(t) \\ \vdots \end{bmatrix}, \quad (58)$$

and

$$\mathbf{Z}_q(t) = \mathbf{P}_q \begin{bmatrix} \mathbf{V}_q(t) \\ \mathbf{V}_q^*(t) \end{bmatrix} = \begin{bmatrix} z_{q,1}(t) \\ z_{q,2}(t) \\ \vdots \end{bmatrix}. \quad (59)$$

In order to make orbital deviations orthogonal to the orbit of the stationary solution, the first dynamical equation in Eq. (56) leads to

$$\dot{\vartheta} = C \exp(i\alpha_0) z_{0,1}(t) \quad (60)$$

and

$$\delta \phi_{0,1} = 0. \quad (61)$$

The correlation properties of the linearly transformed stochastic variables in $\mathbf{Z}_q(t)$ are:

$$\Xi_{m,n}^{(q)} = \langle z_{q,m}^*(t) z_{q,n}(t) \rangle = 2\kappa \Lambda^2 \sum_i \langle \mathcal{P}_{m,i}^{(q)*} \mathcal{P}_{n,i}^{(q)} \rangle, \quad (62)$$

with

$$\mathcal{P}_{m,i}^{(q)*}(t) \mathcal{P}_{n,i}^{(q)}(t) = \mathcal{P}_{m,i}^{(q)*}(0) \mathcal{P}_{n,i}^{(q)}(0). \quad (63)$$

As a consequence, the correlation properties of the linearly transformed modes are obtained as

$$\Pi_{m,n}^{(0)} = \langle \delta \phi_{q,m}^*(t) \delta \phi_{q,n}(t) \rangle = 0 \quad (64)$$

for the cases that $m = 1$ or $n = 1$, and as

$$\Pi_{m,n}^{(q)} = \langle \delta \phi_{q,m}^*(t) \delta \phi_{q,n}(t) \rangle = -\frac{\Xi_{m,n}^{(q)}}{\mathcal{D}_{m,m}^{(q)*} + \mathcal{D}_{n,n}^{(q)}} \quad (65)$$

for the other cases, where $\mathcal{D}_{i,i}^{(q)}$ is the i th diagonal element of \mathbf{D}_q .

Since the eigenvalue 0 only belongs to the 0th block, the Goldstone mode only influences the correlation properties of modes dominated by \mathbf{J}_0 , which are the excited sidemodes in the stationary solution. Although the global phase deviation $\vartheta(t)$ also affects all the other block matrices, it does not affect the value of the correlations.

After recovering $\delta \mathcal{E}(t)$ from $\delta \Phi$ via an inverse linear transformation, we get the average variance of the optical field

fluctuations as

$$\langle |\delta \mathcal{E}_{kL+q}(t)|^2 \rangle = \sum_{m,n} \mathcal{W}_{k+M+1,m}^{(q)*} \mathcal{W}_{k+M+1,n}^{(q)} \Pi_{m,n}^{(q)} \quad (66)$$

for the $(kL+q)$ th mode, and

$$\langle |\delta \mathcal{E}_{kL-q}(t)|^2 \rangle = \sum_{m,n} \mathcal{W}_{k+3M+2,m}^{(q)*} \mathcal{W}_{k+3M+2,n}^{(q)} \Pi_{m,n}^{(q)} \quad (67)$$

for the $(kL-q)$ th mode. Equation (67) only works for the case where q is a positive integer smaller than $L/2$, while Eq. (66) also works for the case with $q = 0$ or $q = L/2$. The results of this orbital deviation analysis for roll patterns are presented in Fig. 4c, d.

Pattern drift and deformation contribution to optical power spectra. The applications of Kerr optical frequency combs are essentially related to their metrological performance. The spectral purity of the comb and of the microwaves that can be generated with them is generally evaluated in terms of phase noise spectra. If we assume that the stationary output signal is $\mathcal{E}_{\text{out},l}(0) = |\mathcal{E}_{\text{out},l}(0)| \exp(i\psi_{s,l})$, the effect of the additive Gaussian white noise is that the instantaneous output optical field exiting the resonator now becomes $\mathcal{E}_{\text{out},l}(t) = (|\mathcal{E}_{\text{out},l}(0)| + \delta E_{\text{out},l}(t)) \exp[i(\psi_{s,l} + \delta \psi_l(t))]$, where $\delta E_{\text{out},l}(t)$ is the real-valued deviation from the initial stationary amplitude and $\delta \psi_l(t)$ is the deviation from the initial stationary phase. The deviation $\delta \psi_l(t)$ is therefore defined as the phase noise and its spectrum is referred to as the phase noise spectrum. We hereafter show that the overall optical phase noise is the sum of two contributions: The first one originates from slow pattern drift and is dominant at low-frequency offset from the carrier; the second one is induced by fast pattern deformation and is dominant at high-frequency offset from the carrier.

We first determine the optical phase noise contribution due to pattern drift, also referred to as global phase deviation. From the previous discussion and calculations, we know this global phase deviation originates from the Goldstone mode with eigenvalue 0. This mode induces a free azimuthal motion for the pattern and, as shown in Eq. (39), the dynamics of the global phase deviation of the soliton is governed by

$$\dot{\vartheta} = C \exp(i\alpha_0) \mathbf{p}_1 \cdot \mathbf{V}(t). \quad (68)$$

This equation is a Wiener process, which here corresponds to a Brownian motion for the phase of the pattern. It is known that in that case the spectrum of the global phase deviation is expressed as²⁸

$$S_{\vartheta}(\omega) = \frac{C^2 \Xi_{1,1}}{\omega^2}. \quad (69)$$

On the other hand, the phase spectrum of the mode l in the comb is expressed as

$$\mathcal{L}_{\mathcal{E},l} = l^2 S_{\vartheta}(\omega) = \frac{l^2 C^2 \Xi_{1,1}}{\omega^2}, \quad (70)$$

while the corresponding power spectral density of the output field $\mathcal{E}_{\text{out},l}$ is

$$S_{\mathcal{E},l}(\omega) = \frac{l^2 C^2 \Xi_{1,1} |\mathcal{E}_{\text{out},l}(0)|^2}{l^4 C^4 \Xi_{1,1}^2 / 4 + \omega^2}. \quad (71)$$

When the additive noise is very small, the phase noise spectrum is related to the power spectra by

$$\mathcal{L}_{\mathcal{E},l} \simeq \frac{S_{\mathcal{E},l}(\omega)}{|\mathcal{E}_{\text{out},l}(0)|^2} \quad (72)$$

except when the offset frequency is too close to the carrier. Meanwhile, since both spectra have very large values near the

carrier frequency, they are expected to be accurate at low offset frequencies. While the effect of Goldstone mode is limited to the fluctuations dominated by the 0th block of the Jacobian for roll patterns, the solutions are exactly the same as the one previously obtained after replacing $\Xi_{1,1}$ with $\Xi_{1,1}^{(0)}$.

We now focus on the optical phase noise contribution due to pattern deformation induced by the sidemode fluctuations. Although the optical phase noise can be obtained from Eq. (21) numerically, we aim at deriving an analytical formula by only accounting for the interaction terms between mode l and 0, while neglecting the remaining ones. We therefore assume that the dynamical equations are

$$\delta\dot{\mathcal{E}}_l = \left[-\kappa + i \left(\sigma - \frac{\zeta_2}{2} l^2 + 2v_g y |\mathcal{E}_0(0)|^2 \right) \right] \delta\mathcal{E}_l + \sqrt{2\kappa\Lambda} v_l(t). \quad (73)$$

This approximation is valid because $|\mathcal{E}_0(0)| \gg |\mathcal{E}_l(0)|$ for $l \neq 0$, and therefore dominates the entire high-frequency spectrum. This approximation also indirectly assumes that the modal fluctuations are independent of each other, i.e., uncorrelated.

We can write the l th non-zero stationary output field as $\mathcal{E}_{\text{out},l}(0) = |\mathcal{E}_{\text{out},l}(0)| \exp(i\psi_{s,l})$ and the corresponding fluctuation as $\delta\mathcal{E}_{\text{out},l}(t) = |\delta\mathcal{E}_{\text{out},l}(t)| \exp(i\psi_{f,l}(t))$. As a consequence, the optical phase noise contribution due to pattern deformation at time t can be approximately written as the projection of $\delta\mathcal{E}_{\text{out},l}(t)$ in the vertical direction of $\mathcal{E}_{\text{out},l}(0)$, in the form

$$\psi_l(t) \simeq \frac{|\delta\mathcal{E}_{\text{out},l}(t)|}{|\mathcal{E}_{\text{out},l}(0)|} \sin(\psi_{f,l} - \psi_{s,l}). \quad (74)$$

The Fourier transform of the projection $|\delta\mathcal{E}_{\text{out},l}(t)| \sin(\psi_{f,l} - \psi_{s,l})$ can now be solved analytically, and we can obtain the spectrum of ψ_b , in the form

$$\mathcal{L}_{\mathcal{E},l} = \frac{2\kappa_t \kappa T_R \Lambda^2}{|\mathcal{E}_{\text{out},l}(0)|^2} \frac{\kappa^2 + \eta_l^2 + \omega^2}{(\kappa^2 + \eta_l^2 - \omega^2)^2 + 4\kappa^2 \omega^2}. \quad (75)$$

The corresponding power spectral density of the field $\mathcal{E}_{\text{out},l}$ may be derived from Eq. (73) as

$$S_{\mathcal{E},l}(\omega) = \frac{4\kappa_t \kappa T_R \Lambda^2}{\kappa^2 + (\omega - \eta_l)^2}. \quad (76)$$

One can note that there is a term of $|\mathcal{E}_{\text{out},l}(0)|^2 \delta(\omega)$ because of the direct current part of $\mathcal{E}_{\text{out},l}(t)$. Although most of the additive noise drives the orbital deviation, we know that the pattern drift noise is large at low-frequency offset and this model is only intended to be valid for high-frequency offset. Therefore, this zero-frequency term is omitted in the above equation. This approach is valid for both soliton and roll patterns.

Figure 5 displays the excellent agreement between our analytical predictions and the numerical simulations. It can be seen that for small frequency offsets, the numerical simulations agree well with the pattern drift contribution of phase noise. Conversely, for large frequency offsets, the numerical simulations agree instead with the pattern deformation contribution of phase noise. The pattern drift sidemode spectra in Eq. (71) depends on the sidemode amplitude, while the pattern deformation sidemode spectra in Eq. (76) does not. As a consequence, there is a notable difference when we compare the spectra for different sidemodes of the roll pattern. However, for solitons, the amplitude of the sidemode decreases slower with the increase of $|l|$, so that the change is not so large.

Pattern drift and deformation contribution to microwave phase noise. Microwave generation using Kerr combs is obtained

via a process of photodetection. The spectral purity of these microwaves is generally evaluated in terms of phase noise spectra^{12,29–32}. For the sake of simplicity, we here consider an ideal photodetector, so that the noise properties of the generated microwave can be solely attributed to the comb. The photodetector extracts the power envelope of the output field and generates a radio-frequency signal that is proportional to the incoming optical power following $V_{\text{PD}}(t) = S|\mathcal{E}_{\text{out}}|^2$ (in units of Volts), where S is the responsivity of the photodetector (in units of VW^{-1}), while

$$\mathcal{E}_{\text{out}} = \sum_l \mathcal{E}_{\text{out},l} \exp(il\Omega_R t). \quad (77)$$

This signal can be Fourier-expanded in the form

$$V_{\text{PD}}(t) = \frac{1}{2} \mathcal{M}_0 + \sum_{n=1}^{+\infty} \left[\frac{1}{2} \mathcal{M}_n \exp(in\Omega_R t) + \text{c.c.} \right], \quad (78)$$

where the spectral components

$$\mathcal{M}_n = 2S \sum_m \mathcal{E}_{\text{out},m}^* \mathcal{E}_{\text{out},m+n} \quad (79)$$

are the complex-valued envelopes of the microwave harmonics of frequency $n \times \Omega_R$, and c.c. stands for the complex conjugate^{33,34}.

We can now evaluate the effect of pattern drift on microwave phase noise. The slowly varying envelope of the microwave spectral component of frequency $n\Omega_R$ in a noiseless situation can be written as $\mathcal{M}_n(0) = 2S \sum_l \mathcal{E}_{\text{out},l+n}(0) \mathcal{E}_{\text{out},l}^*(0)$ with $\mathcal{E}_{\text{out},l}(0) = \sqrt{2\kappa_t T_R} \mathcal{E}_l(0) - \sqrt{P_L} \delta(l)$. Pattern drift induced by global phase deviation modifies the slowly varying envelope of the n th microwave component as

$$\mathcal{M}_n = \mathcal{M}_n(0) \exp[in\vartheta(t)]. \quad (80)$$

For solitons, n could be any positive integer and the spectrum of the microwave phase noise is

$$\mathcal{L}_{\mathcal{M},n}(\omega) = n^2 S_g(\omega) = \frac{n^2 C^2 \Xi_{1,1}}{\omega^2}, \quad (81)$$

while the corresponding power spectrum is

$$S_{\mathcal{M},n}(\omega) = \frac{n^2 C^2 \Xi_{1,1} |\mathcal{M}_n(0)|^2}{l^4 C^4 \Xi_{1,1}^2 / 4 + \omega^2} \quad (82)$$

$$\simeq |\mathcal{M}_n(0)|^2 \mathcal{L}_{\mathcal{M},n}(\omega). \quad (83)$$

For roll patterns, n must be a positive multiple of L and the formulas for the drift-induced microwave spectrum are the same, except that $\Xi_{1,1}$ is replaced by $\Xi_{1,1}^{(0)}$.

With respect to the effect of pattern deformation on microwave phase noise, one can first note that the effect of modal fluctuations on the slowly varying envelope of the microwave spectral component of frequency $n\Omega_R$ is expressed as

$$\mathcal{M}_n = 2S \sum_l \mathcal{E}_{\text{out},l+n} \mathcal{E}_{\text{out},l}^* \quad (84)$$

$$\simeq 2S \sum_l \left[\mathcal{E}_{\text{out},l+n}(0) \delta\mathcal{E}_{\text{out},l}^* + \delta\mathcal{E}_{\text{out},l+n} \mathcal{E}_{\text{out},l}^*(0) \right] + \mathcal{M}_n(0). \quad (85)$$

Using the formula for optical phase noise spectra as derived in Eq. (75), we obtain the following formula for the microwave

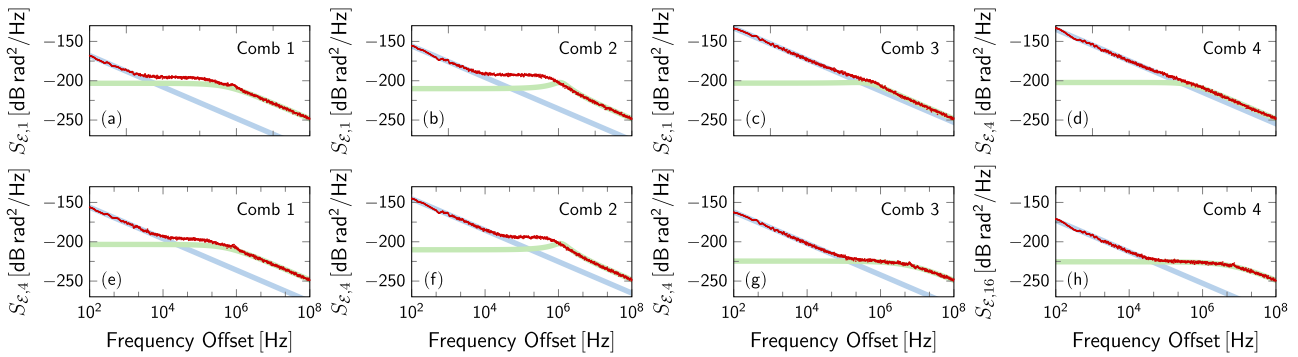


Fig. 5 Sidemode spectra of the output optical field. **a–d** Spectra of excited sidemodes that are closest to the right of the center mode. **e–h** Spectra of excited sidemodes that are fourth closest to the right of the center mode. The figure corresponds to Combs 1 to 4 displayed in Fig. 2. The blue lines correspond to the noise contribution of pattern drift [the computation of Eq. (71)]. The green lines correspond to the noise contribution of pattern deformation [the computation of Eq. (76)]. The red lines correspond to the spectra obtained after the numerical simulation of the stochastic modal equations. These simulations clearly indicate that pattern drift noise dominates the spectra for low offset frequencies, while pattern deformation noise dominates the spectra for high offset frequencies.

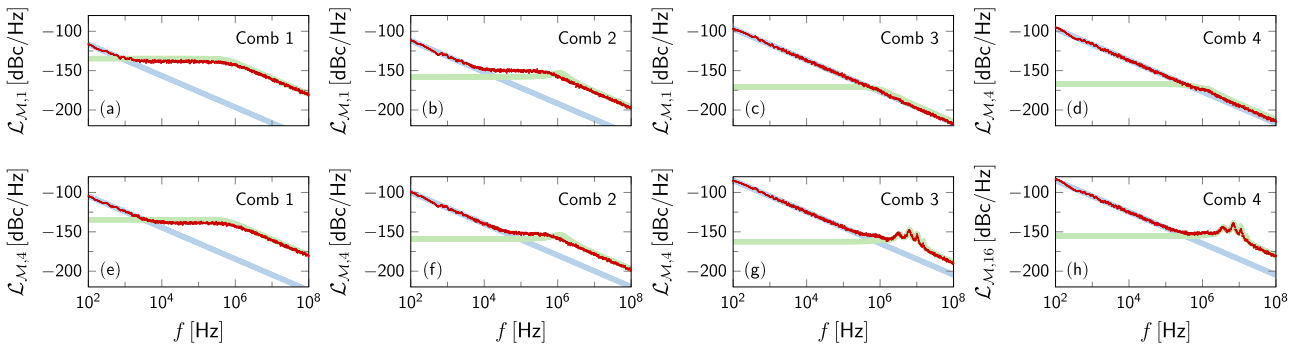


Fig. 6 Phase noise spectra of the microwaves. **a–d** Phase noise spectra of the microwaves with the lowest frequency. **e–h** Phase noise spectra of the microwaves with the fourth lowest frequency. The figure corresponds to the results obtained via photodetection of Combs 1 to 4 displayed in Fig. 2. The simulation results (redline) are obtained from the simulation of Eq. (1). The blue lines correspond to pattern drift noise [the computation of Eq. (81)] while the green lines correspond to pattern deformation noise [the computation of Eq. (86)]. The numerical simulations show that, as in the case of optical noise, pattern drift noise dominates the spectra for low offset frequencies, while pattern deformation noise dominates the spectra for high offset frequencies.

phase noise spectrum:

$$\begin{aligned} \mathcal{L}_{M,n}(\omega) &= \frac{8\kappa_t \kappa T_R \Lambda^2 S^2}{|M_n|^2} \\ &\times \sum_l [|\mathcal{E}_{\text{out},l+n}(0)|^2 + |\mathcal{E}_{\text{out},l-n}(0)|^2] \\ &\times \frac{(\kappa + \eta_l^2 + \omega^2)}{(\kappa^2 + \eta_l^2 - \omega^2)^2 + 4\kappa^2 \omega^2}. \end{aligned} \quad (86)$$

while the corresponding power spectrum is given by

$$S_{M,n}(\omega) = 16\kappa_t \kappa T_R \Lambda^2 S^2 \times \sum_l \left[\frac{|\mathcal{E}_{\text{out},l+n}(0)|^2}{\kappa^2 + (\omega + \eta_l)^2} + \frac{|\mathcal{E}_{\text{out},l-n}(0)|^2}{\kappa^2 + (\omega - \eta_l)^2} \right]. \quad (87)$$

The term of $|M_n(0)|^2 \delta(\omega)$ is omitted in the above equation because this model is intended to describe high-frequency fluctuations. Here again, these equations are valid for both solitons and roll patterns. For solitons, n could be any positive integer, while for roll patterns, n must be a positive multiple of L .

The solution of the simulation and analytical results for the generated microwaves are shown in Fig. 6. It can be seen that the pattern drift spectra are always very accurate at low offset frequencies because the global phase deviation dominates in that frequency range. On the other hand, the numerical simulations converge to pattern deformation spectra at high

frequencies because it is the range corresponding to the fast field fluctuations. The pattern deformation spectra model predicts the potential existence of one or several peaks near the frequency of overall detuning η_l while the pattern drift spectra do not have any. Similarly to Fig. 5, by comparing phase noise spectra for different microwave components in the same comb, we can see the difference is larger in roll patterns.

Finally, we note that there is a point around or below the half-linewidth of the resonator κ where the transition between the drift and deformation spectra occurs. This transition should be set at the frequency at which the spectral lines predicted by the two models intersect. From our simulation, we find that this transition frequency is ~ 1 MHz for roll patterns, while for bright and dark solitons, the transition frequency can be much lower, down to the 10 kHz frequency range.

Conclusion

In this communication, we have investigated the phase noise of microwaves generated with Kerr optical frequency combs driven by additive Gaussian noise. We have used a theoretical approach based on stochastic coupled mode equations to determine phase noise spectra in the optical and microwave domains. Our analysis has shown that there are two dominant contributions to the phase noise spectra. The first one is pattern drift, which corresponds to the slow Brownian motion of the patterns in the azimuthal direction and it is dominant at low

offset frequencies. The second contribution is pattern deformation, associated with the fast stochastic changes in the shape of the intracavity patterns. The transition between both contributions occurs around or below the resonance linewidth frequency.

Our emphasis here has been on whispering-gallery mode resonators with high quality factors. However, a similar analysis will apply to any resonator whose dynamics is governed by the coupled mode equations or the Lugiato-Lefever equation and in which the noise bandwidth can be considered white over the linewidth of the resonator modes. Relatively little work has been done on non-white noise sources in systems that are governed by the nonlinear Schrödinger equation at the lowest order, including systems that are governed by the coupled mode equations or the Lugiato-Lefever equation. Non-white noise sources are important in microresonators, and this subject is an important topic for future research. Future work will also address the effects of photodetector noise, optical multiplicative noise, and be on mapping the phenomenological noise amplitudes to known intracavity fluctuations, such as thermal expansion or thermorefractive noise.

Methods

Numerical simulations are performed by integrating the stochastic coupled-mode equations in Eq. (1) using the fourth-order Runge-Kutta method in MATLAB. The numerical calculations of the nonlinear terms are optimized by the fast Fourier transform algorithm shown in ref. ³⁵. We first compute the stationary solution without noise, and then add Gaussian white noise terms to the simulation of the dynamics. The global phase deviation $\vartheta(t)$ is tracked in the calculation by numerical integration of Eq. (68), while the phase noise is derived by calculating the difference between the phase of the output signal and the phase of the initial stationary solution. The phase noise spectra are simulated with a Hanning window $H_w(t) = \sqrt{8/3} \sin^2(\pi t/T)$, where T is the temporal width of the window²⁸.

Data availability

The data that support the findings of this paper are available from the corresponding author upon reasonable request.

Code availability

The codes that support the findings of this paper are available from the corresponding author upon reasonable request.

Received: 6 November 2022; Accepted: 27 April 2023;

Published online: 25 May 2023

References

- Kippenberg, T. J., Holzwarth, R. & Diddams, S. A. Microresonator-based optical frequency combs. *Science* **332**, 555 (2011).
- Gaeta, A. L., Lipson, M. & Kippenberg, T. J. Photonic-chip-based frequency combs. *Nat. Photon.* **13**, 158 (2019).
- Savchenkov, A. A. et al. Low threshold optical oscillations in a whispering gallery mode CaF₂ resonator. *Phys. Rev. Lett.* **93**, 243905 (2004).
- Kippenberg, T. J., Spillane, S. M. & Vahala, K. J. Kerr-nonlinearity optical parametric oscillation in an ultrahigh-Q toroid microcavity. *Phys. Rev. Lett.* **93**, 083904 (2004).
- Strekalov, D. V., Marquardt, C., Matsko, A. B., Schwefel, H. G. L. & Leuchs, G. Nonlinear and quantum optics with whispering gallery resonators. *J. Opt.* **18**, 123002 (2016).
- Lin, G., Coillet, A. & Chembo, Y. K. Nonlinear photonics with high-Q whispering-gallery-mode resonators. *Adv. Opt. Photon.* **9**, 828 (2017).
- Pasquazi, A. et al. Micro-combs: a novel generation of optical sources. *Phys. Rep.* **729**, 1 (2018).
- Pfeifle, J. et al. Optimally coherent Kerr combs generated with crystalline whispering gallery mode resonators for ultrahigh capacity fiber communications. *Phys. Rev. Lett.* **114**, 093902 (2015).
- Picqué, N. & Hänsch, T. W. Frequency comb spectroscopy. *Nat. Photon.* **13**, 146–157 (2019).
- Suh, M. G. & Vahala, K. J. Soliton microcomb range measurement. *Science* **359**, 884–887 (2018).
- Trocha, P. et al. Ultrafast optical ranging using microresonator soliton frequency combs. *Science* **359**, 887–891 (2018).
- Li, J., Lee, H., Chen, T. & Vahala, K. J. Low-pump-power, low-phase noise, and microwave to millimeter-wave repetition rate operation in microcombs. *Phys. Rev. Lett.* **109**, 233901 (2012).
- Matsko, A. B., Savchenkov, A. A., Yu, N. & Maleki, L. Whispering-gallery-mode resonators as frequency references. I. Fundamental limitations. *JOSA B* **24**, 1324–1335 (2007).
- Savchenkov, A. A., Matsko, A. B., Ilchenko, V. S., Yu, N. & Maleki, L. Stabilization. *JOSA B* **24**, 2988–2997 (2007).
- Huang, G. et al. Thermorefractive noise in silicon-nitride microresonators. *Phys. Rev. Lett.* **99**, 061801 (2019).
- Chembo, Y. K., Strekalov, D. V. & Yu, N. Spectrum and dynamics of optical frequency combs generated with whispering gallery mode resonators. *Phys. Rev. Lett.* **104**, 103902 (2010).
- Chembo, Y. K. & Yu, N. Modal expansion approach to optical-frequency-comb generation with monolithic whispering-gallery-mode resonators. *Phys. Rev. A* **82**, 033801 (2010).
- Matsko, A. B. et al. Mode-locked Kerr frequency combs. *Opt. Lett.* **36**, 2845–2847 (2011).
- Chembo, Y. K. & Menyuk, C. R. Spatiotemporal Lugiato-Lefever formalism for Kerr-comb generation in whispering-gallery-mode resonators. *Phys. Rev. A* **87**, 053852 (2013).
- Coen, S., Randle, H. G., Sylvestre, T. & Erkintalo, M. Modeling of octave-spanning Kerr frequency combs using a generalized mean-field Lugiato-Lefever model. *Opt. Lett.* **38**, 37–39 (2013).
- Lugiato, L. A., Prati, F., Gorodetsky, M. L. & Kippenberg, T. J. From the Lugiato-Lefever equation to microresonator-based soliton Kerr frequency combs. *Philos. Trans. R. Soc. A* **376**, 20180113 (2018).
- Chembo, Y. K., Coillet, A., Lin, G., Colet, P. & Gomila, D. Fluctuations and correlations in Kerr optical frequency combs with additive Gaussian noise. *Chaos* **30**, 083146 (2020).
- Menyuk, C. R. & Wang, S. Spectral methods for determining the stability and noise performance of passively modelocked lasers. *Nanophotonics* **5**, 332–350 (2016).
- Wang, S., Carruthers, T. F. & Menyuk, C. R. Efficiently modeling the noise performance of short-pulse lasers with a computational implementation of dynamical methods. *JOSA B* **35**, 2521–2531 (2018).
- Wang, S. et al. Wake mode sidebands and instability in mode-locked lasers with slow saturable absorbers. *Opt. Lett.* **42**, 2362–2365 (2017).
- Demir, A., Mehrotra, A. & Roychowdhury, J. Phase noise in oscillators: a unifying theory and numerical methods for characterization. *IEEE Trans. Circuits Syst. I Fundam. Theory Appl.* **47**, 655–674 (2000).
- Lin, G. et al. Subharmonic instabilities in Kerr microcombs. *Opt. Lett.* **48**, 578–581 (2023).
- Kasdin, N. J. Discrete simulation of colored noise and stochastic processes and $1/f^\alpha$ power law noise generation. *Proc. IEEE* **83**, 802–827 (1995).
- Liang, W. et al. High spectral purity Kerr frequency comb radio frequency photonic oscillator. *Nat. Commun.* **6**, 7957 (2015).
- Huang, S.-W. et al. A low-phase-noise 18 GHz Kerr frequency microcomb phase-locked over 65 THz. *Sci. Rep.* **5**, 13355 (2015).
- Saleh, K. & Chembo, Y. K. On the phase noise performance of microwave and millimeter-wave signals generated with versatile Kerr optical frequency combs. *Opt. Express* **24**, 25043 (2016).
- Lucas, E. et al. Ultralow-noise photonic microwave synthesis using a soliton microcomb-based transfer oscillator. *Nat. Commun.* **11**, 374 (2020).
- Diallo, S. & Chembo, Y. K. Optimization of primary Kerr optical frequency combs for tunable microwave generation. *Opt. Lett.* **42**, 3522 (2017).
- Nguewou-Hyousse, H. & Chembo, Y. K. Stochastic analysis of miniature optoelectronic oscillators based on whispering-gallery mode electrooptical modulators. *IEEE Photon. J.* **13**, 3000110 (2021).
- Hansson, T., Modotto, D. & Wabnitz, S. On the numerical simulation of Kerr frequency combs using coupled mode equations. *Opt. Commun.* **312**, 134–136 (2014).

Acknowledgements

This research was funded by the Air Force Office of Scientific Research (AFOSR Grant FA9550-20-1-0357).

Author contributions

F.L. and Y.K.C. developed the theoretical model. F.L. performed the numerical simulations. F.L., C.R.M., and Y.K.C. discussed the results, analyzed the data, and wrote the manuscript. Y.K.C. proposed the idea and supervised the project.

Competing interests

The authors declare no competing interests.

Additional information

Correspondence and requests for materials should be addressed to Yanne K. Chembo.

Peer review information *Communications Physics* thanks the anonymous reviewers for their contribution to the peer review of this work.

Reprints and permission information is available at <http://www.nature.com/reprints>

Publisher's note Springer Nature remains neutral with regard to jurisdictional claims in published maps and institutional affiliations.



Open Access This article is licensed under a Creative Commons Attribution 4.0 International License, which permits use, sharing, adaptation, distribution and reproduction in any medium or format, as long as you give appropriate credit to the original author(s) and the source, provide a link to the Creative Commons license, and indicate if changes were made. The images or other third party material in this article are included in the article's Creative Commons license, unless indicated otherwise in a credit line to the material. If material is not included in the article's Creative Commons license and your intended use is not permitted by statutory regulation or exceeds the permitted use, you will need to obtain permission directly from the copyright holder. To view a copy of this license, visit <http://creativecommons.org/licenses/by/4.0/>.

© The Author(s) 2023